JAAS

ROYAL SOCIETY OF CHEMISTRY

PAPER

View Article Online
View Journal

Cite this: DOI: 10.1039/d3ja00358b

(LA)-MC-ICPMS/MS measurement of Sr radiogenic isotope ratios†

Philippe Télouk and Vincent Balter *

A prefiltering system made up of a double-Wien filter and a collision/reaction cell is included with the new Neoma MC-ICPMS/MS to reduce spectral interferences and allow high-precision isotope analyses. In the present study, we challenge these capabilities for measuring Sr isotopes. We first test the effect of different combinations of magnetic and electrostatic field values in the double-Wien filter on the transmission of a bandpass window that includes Sr isotopes and their reaction products. We next scrutinize the spectrum of ion products resulting from the introduction of N_2O or SF_6 to remove on-line Rb which interferes with Sr on the 87-mass unit. While N_2O is the preferred reaction gas when using ICPMS/MS, we found that it reacts with Sr to create expected $Sr^{16}O$ products, but also ^{14}N- and, most probably, ^{18}O-based interfering products. By contrast, the introduction of SF_6 generates a more resolved spectrum of F-based products, notably because F is mono-isotopic, but leads to a 50% reduction in signal intensity. Care must, however, be taken to measure $^{88}SrF^+$ in a mass range free of the $^{32}S^{19}F_3{}^{16}O^+$ interference. We then measure the $^{87}SrF/^{86}SrF$ ratio first in raw solutions of a suite of geological reference materials without prior Sr extraction and second in sintered in-house materials and natural solid samples using laser ablation. In the solution mode, no RbF^+ is detectable and the sensitivity is ~50 V ppm^{-1} for $^{88}SrF^+$. The accurate measurements of the $^{87}SrF/^{86}SrF$ ratio of the geological reference materials are achieved with an uncertainty of 70 ppm (±2 SD), which is comparable with that typically obtained using MC-ICPMS with prior Sr extraction. In the laser ablation mode, the performance without SF_6 of the Neoma for measuring Sr isotopes in homogeneous materials is roughly equivalent to that of the Neptune MC-ICPMS. With SF_6, the Neoma MS/MS exhibits a sensitivity of ~8 mV ppm^{-1} (based on ^{88}SrF) and the measurement of the $^{87}SrF/^{86}SrF$ ratio has a short-term external precision of ~0.0015 (±2 SD). Finally, an analysis of a heterogeneous material (a fossil tooth) reveals more well-resolved spatial variations of the $^{87}SrF/^{86}SrF$ ratio than of the $^{87}Sr/^{86}Sr$ ratio, likely thanks to the absence of $^{87}RbF^+$.

Received 20th October 2023
Accepted 18th January 2024

DOI: 10.1039/d3ja00358b

rsc.li/jaas

1 Introduction

Recently, the field of multi-collection inductively coupled plasma mass spectrometry (MC-ICPMS) has seen the commercialization of a new type of instrument incorporating a collision/reaction cell (CRC) module to reduce polyatomic interfering species. The principle of a CRC is based on (i) the preferential collision of a polyatomic interfering species with a gas due to a larger collisional cross section than analytes, or (ii) the selective chemical reaction of an analyte or its interfering species with a gas.[1] Collisions result in a loss of energy (also known as kinetic energy dispersion) for polyatomic species that decelerate and are removed from the ion beam thanks to a bias voltage at the end of CRC.[1] In the CRC, the ion beam is kept focused with a hexapole that reduces ion scattering without impeding ion transmission.[1] Reactions result in the mass shift of an analyte or its interfering species, which no longer have isobaric overlap. Reactions can also result in asymmetric charge transfer from an interfering species, which becomes neutral, to the gas. The first attempt to incorporate a CRC into an ICPMS instrument dates to mid-1990s[2] and into a MC-ICPMS with the IsoProbe (GV Instruments, Manchester, UK) to the 2000s.[3] In 2017, the Sapphire CRC-MC-ICPMS was released by Nu Instruments (Wrexham, UK), which is a dual-path MC-ICPMS with a CRC installed on the low energy path.[4–6] More recently in 2022, an alternative instrument, the Neoma MC-ICPMS/MS was commercialized by Thermo Scientific (Bremen, Germany).

The MS/MS prefiltering technology embarked in the Neoma consists of a double-Wien filter and a CRC.[7–9] Briefly, the double-Wien filter works by deflecting ions away from the axial trajectory in the first filter and refocusing them back towards the axial trajectory in the second filter, both depending on the ion velocity. Similar in structure, the two Wien filters allow an ion beam to pass through an arrangement of a uniform electrostatic ($\vec{E}$) field orthogonal to a magnetic ($\vec{B}$) field, which will deflect ions

LGL-TPE, UMR 5276, CNRS, Ecole Normale Supérieure de Lyon, Université de Lyon 1, 9, rue du Vercors, 69342 Lyon cedex 07, France. E-mail: Vincent.Balter@ens-lyon.fr

† Electronic supplementary information (ESI) available. See DOI: https://doi.org/10.1039/d3ja00358b

according to their velocity. The axial transmission of an ion m_0 with a velocity v_0 will happen when $v_0 = \overrightarrow{|E|} / \overrightarrow{|B|}$ (or $v_0 = E/B$), but ions with a too large mass-to-charge (m/z) difference relative to m_0/z will not be selected using an adjustable slit located between the two Wien filters. Thus, a certain mass range can be transmitted through a double-Wien filter using a combination of E, B, and adjustable slit aperture (S) values. The units currently used are % for the magnetic field B value (100% corresponds to 0.63 T), V for the electrostatic field E value, and % for the slit aperture S value (100% is full open). As a general rule, increasing the B (while keeping E/B constant) and reducing S values leads to the asymmetric steepening and narrowing of the bandpass window, with higher efficiency at removing low masses than high masses.[9] After being focused by several lenses, the ion beam exits the double-Wien filter to the CRC. In summary, the double-Wien prefiltering allows a neater ion beam to enter the CRC, therefore reducing potential spectral and matrix interferences.

The incorporation of a CRC into MC-ICPMS instruments is therefore promising at removing argide-based interferences in solution for precise Ca,[10–12] K,[13–15] Fe[16] and Cu[9] isotope compositions. It is also promising for laser ablation (LA) applications, for which the analyte is combined with the matrix sample and can be separated on-line using a CRC. A classical application is the separation of $^{87}Sr^+$ from $^{87}Rb^+$, primarily for Rb–Sr dating but also for other purposes. Starting from an initial value of ~0.699 in chondrites,[17] the $^{87}Sr/^{86}Sr$ ratio evolved through time with the radioactive decay of ^{87}Rb -> ^{87}Sr ($t_{1/2} = 49.61 \pm 0.16$ Ga) and through geochemical partitioning between Rb, a K-like monovalent alkali metal, and Sr, a Ca-like divalent alkaline-earth metal, resulting in a typical ~15% variation of the $^{87}Sr/^{86}Sr$ value in geological materials. This large range of the $^{87}Sr/^{86}Sr$ value has been used for years for different applications, from cosmochemistry,[17,18] mantle and crust geochemistry,[19,20] isotope stratigraphy,[21,22] human and animal past mobility,[23,24] archaeological artifact provenance,[25,26] to forensics[27,28] and goods of value authentication.[29,30]

The mass-shift reaction of Sr^+, which has a s^1 electron configuration, is the basis for the on-line chemical resolution of $^{87}Sr^+$ and $^{87}Rb^+$, whereas Rb^+, which has a s^0 electron configuration, is much more inert to the process. The use of SrF^+ reaction product ions for separating $^{87}Sr^+$ from $^{87}Rb^+$ was pioneered more than two decades ago, first using CH_3F.[31] In a subsequent methodical survey, different gases, N_2O, CO_2, D_2O, CH_3F, SF_6, CH_3Cl, CS_2, and NH_3, were tested to separate $^{87}Sr^+$ from $^{87}Rb^+$, of which N_2O, and SF_6, exhibit the highest reactivity.[32] The first use of LA-ICPMS/MS for Rb–Sr dating was first reported in 2016[33,34] and further deployed most generally using N_2O as the reaction gas[35–37] on the basis that resulting signal intensities of SrO^+ are higher than SrF^+.[38] However, SF_6 is preferred as the reaction gas for Rb–Sr dating when using LA-MC-ICPMS/MS because monoisotopic F ensures that SrF^+ reaction product ions do not isomerically interfere with each other.[7,8,39]

Previous works describing the capability of the Proteus (Thermo Scientific, Bremen, Germany) or the Neoma MC-ICPMS/MS for dating purposes using the ^{87}Rb–^{87}Sr systematics with LA have already been reported.[7,8,39] The present work aims at exploring the performance of the Neoma MC-ICPMS/MS instrument to measure the $^{87}Sr/^{86}Sr$ ratio in raw solutions or solid materials.

2 Experimental

2.1 Reagents and materials

All experiments were carried out in laminar flow hoods in a clean laboratory at the LGL-TPE (Ecole Normale Supérieure de Lyon). Acids (HNO_3, HCl, and HF) were double distilled to reduce blank contamination. Ultrapure water (resistivity > 18.2 MΩ·cm) was obtained from a Milli-Q Element water purification system (Merck Millipore, Bedford, MA, USA). The performance of the double-Wien prefiltering was assessed using the multi-element standard solution SCP33MS containing 33 elements (SCP Sciences, Québec, Canada) diluted at 200 ng ml^{-1}. Mass scans were performed from 20 to 250 atomic mass units (amu) with an axial value m_0 set at ^{96}Mo, *i.e.*, at the middle of the mass range between 85 amu (^{85}Rb) and 107 amu ($^{88}Sr^{19}F$) to check the ion mass range entering the instrument at different B values while keeping the E/B ratio and S at 5–6 and 70%, respectively. For solution measurements, ten geological certified reference materials (CRM) were obtained from the United States Geological Survey (USGS), the Geological Survey of Japan (GSJ), and the Centre de Recherches Pétrographiques et Géochimiques (CRPG), whose information is summarized in Table 1.[40–45] A minimum sample size of 100 mg was weighed for CRM to avoid measurement uncertainties due to the heterogeneity of the reference material powder. Certified reference materials were digested with a mixture of 5 ml of 27 M distilled HF and 2.5 ml of 15 M distilled HNO_3 at 120 °C for 12 hours and evaporated to dryness. Fluorides were redissolved using 2 ml of 6 M HCl and heated on a hotplate at 100 °C for 12 hours, and then evaporated to dryness. The references $^{87}Sr/^{86}Sr$ value for these CRM were extracted from the GeoReM database.[41] For LA measurements, eleven sintered powder hydroxylapatite or calcite materials and three monocrystalline fluorapatite (FAP) samples were studied, whose information is given in Table 1. Once sintered,[40] the pellets were micro-sampled for measuring the $^{87}Sr/^{86}Sr$ in solution mode to serve as reference values. Strontium was extracted following the procedure elaborated by Guiserix *et al.*[46] Additionally, the $^{87}SrF/^{86}SrF$ ratio was measured in two fossil teeth to investigate the effect of Sr fluorination and to generate, for the first time to the best of our knowledge, a centimeter-wide map.

2.2 Instrumentation

Different instruments and different modes (solution, LA) are used to measure the $^{87}Sr/^{86}Sr$ or the $^{87}SrF/^{86}SrF$ ratios. Table 2 gives a summary of these parameters. All the cup configurations are given in Table 3 depending on the laboratory and the instrument. The pre-commercial Neoma MC-ICPMS/MS at Bremen was used in LA mode, and the commercialized Neoma at Lyon was used in both modes. A 193NWR (Elemental Scientific Lasers, Omaha, NE) was connected to the Neoma MC-ICPMS/MS both at Bremen and Lyon. We also used a Nu Plasma MC-ICPMS (Nu Instruments, Wrexham, UK) and a Neptune MC-ICPMS (Thermo Scientific, Bremen, Germany).

Table 1 List and description of the samples measured for $^{87}Sr/^{86}Sr$ and/or $^{87}SrF/^{86}SrF$ ratios, which values are given in Table S1. The full description of the sample can be found in the corresponding reference (ref.), and the corresponding experiment (exp. #) described in the text

Exp. #	Sample ID	Description	Ref.
#1	BCR-1	Basalt, Columbia River, WA (USGS)	41
	BHVO-1	Basalt, Kilauea, HI (USGS)	41
	BE-N	Basalt, Essey-la-Côte, France (CRPG)	41
	JB-1a	Basalt, Sasebo, Japan (GSJ)	41
	BIR-1	Basalt, Reykjavik, Iceland (USGS)	41
	JA-3	Andesite, Gunma, Japan (GSJ)	41
	AGV2	Andesite, Guano Valley, OR (USGS)	41
	DNC-1	Dolerite, Braggstown, NC (USGS)	41
	JG-3	Granodiorite, Simane, Japan (GSJ)	41
	W2	Diabase, Centerville, VA (USGS)	41
#2	SRM915B	SPS sintered powder NIST SRM-915b “Ca carbonate”	40
	SRM1400	SPS sintered powder NIST SRM-1400 “Bone ash”	42
	MAPS4	SPS sintered pellet USGS synthetic HAP	43
	MAPS5	SPS sintered pellet USGS synthetic HAP	43
	HAPp1	SPS sintered powder synthetic HAP	40
	HAPp2	SPS sintered powder synthetic HAP	40
	BA1	SPS sintered bone powder of extant whale	—
	MN16	SPS sintered fossil bone powder from Iwelen, *ca.* 3 ka, Niger	44
	H6	SPS sintered fossil bone powder from Saint-Césaire, *ca.* 35 ka, France	45
	AZE2	SPS sintered fossil bone powder from Azé, *ca.* 300 ka, France	44
	Chi	SPS sintered fossil bone powder from Chilhac, *ca.* 2 Ma, France	—
	PRT-1	Natural igneous monocrystalline FAP, Portugal	—
	MD1, MD2, MD3	Natural igneous monocrystalline FAP, Madagascar	—
	BRM	Natural igneous monocrystalline FAP, Burma	40
#3		Fossil tooth of protocetid whale from Dagbati, *ca.* 45 Ma, Togo	—

Table 2 Tune parameters for Sr isotope analyses for all instruments

	Solution		Laser		
	Neoma MS/MS Lyon	Nu plasma Lyon	Neoma MS/MS Lyon	Neoma (MS/MS) Bremen	Neptune Lyon
Laser ablation					
Spot diameter (mm)			100	100	100
Fluence (J cm^{-2})			6	6	6
Repetition rate (Hz)			50	20	20
Speed (mm s^{-1})			100	60	60
He (L min^{-1})			1	1	1
Plasma					
RF power (W)	1200	1350	1200	1200	1200
Plasma condition	Wet, quartz cyclonic/scott double spray chamber	Wet, cyclonic spray chamber			
Nebulizer Ar flow (L min^{-1})	0.9	35			
Sampling cone	Standard	Ni	Jet	Jet	Jet
Skimmer cone	H	Ni	X	X	X
MS/MS					
Magnetic field	50		50	50	
Electrostatic field	295		295	320	
Slit aperture (%)	70		70	50	
SF_6 (L min^{-1})			0.12	0.24	
Collection					
Sensitivity (V ppm^{-1})	^{88}SrF ~30	(^{88}Sr) ~27	0.008	0.008	0.015
Blank signal (2% HNO_3)	^{88}SrF ~6 mV	^{88}Sr ~3.5 mV			
Integration time (s)	4.194	10	0.01	1	0.134
Cycles	40	40			

Table 3 Cup configurations for Sr isotope analyses for all instruments. For each combination of laboratory (lab.) and instrument (inst.), a configuration (config. §) number is reported in the text for simplicity

			Cup											
Lab., inst. (config. §)	Mode	Cycle	L5	L4	L3	L2	L1	C	H1	H2	H3	H4	H5	H6
Lyon, Neoma (§1)	Solution	Rb + SrF	^{85}Rb	^{86}Sr	^{87}Rb + ^{87}Sr	^{88}Sr			^{84}SrF	^{85}RbF	^{86}SrF	^{87}SrF	^{88}SrF	
Lyon, Neoma (§2a)	Solution	SrF		^{82}KrF	^{83}KrF	^{84}SrF	^{85}RbF	^{86}SrF	^{87}SrF	^{88}SrF				
Bremen, Lyon, Neoma (§2b)	Laser	SrF		^{82}KrF	^{83}KrF	^{84}SrF	^{85}RbF	^{86}SrF	^{87}SrF	^{88}SrF				
Lyon, Neoma (§3a)	Laser	Rb + Sr		^{82}Kr	^{83}Kr	^{84}Sr	^{85}Rb	^{86}Sr	^{87}Rb+^{87}Sr	^{88}Sr				
Lyon, Neptune (§3b)	Laser	Rb + Sr		^{82}Kr	^{83}Kr	^{84}Sr	^{85}Rb	^{86}Sr	^{87}Rb+^{87}Sr	^{88}Sr				
Lyon, Nu plasma 500 (§4)	Solution	Rb + Sr	^{84}Sr	^{85}Rb	^{86}Sr	^{87}Rb + ^{87}Sr		^{88}Sr				^{90}Zr	^{91}Zr	^{92}Zr

The first instrument was used in solution mode to measure the $^{87}Sr/^{86}Sr$ ratio of the Sr fraction isolated from pellets following the procedure described by Guiserix *et al.*[46] The second instrument was used in the LA mode to measure the $^{87}Sr/^{86}Sr$ ratio in pellets following the procedure described by Rivollat *et al.*[47]

For the Neoma using the CRC, sample (s) measured (m) $^{87}SrF/^{86}SrF$ ratios (s,m) were corrected for instrumental mass bias (β_{Sr}) to obtain normalized $^{87}SrF/^{86}SrF$ ratios (s,n) using an exponential fractionation law following the equations,

$$\left(\frac{^{87}SrF}{^{86}SrF}\right)_{s,n} = \left(\frac{^{87}SrF}{^{86}SrF}\right)_{s,m} \times \left(\frac{M^{87}Sr}{M^{86}Sr}\right)^{\beta_{Sr}} \quad (1)$$

With

$$\beta_{Sr} = \frac{Ln\left(\left(\frac{^{88}Sr}{^{86}Sr}\right)_t \Big/ \left(\frac{^{88}SrF}{^{86}SrF}\right)_{s,m}\right)}{Ln\left(\frac{M^{86}Sr}{M^{88}Sr}\right)} \quad (2)$$

where $M^{88,87,86}Sr$ correspond to the atomic masses of the corresponding isotopes and $(^{88}Sr/^{86}Sr)_t$ the true $^{88}Sr/^{86}Sr$ ratio (8.375209) conventionally used for internal normalization of Sr isotopic ratios. Eqn (1) implicitly assumes that instrumental mass bias impacts Sr isotopes rather than SrF isotopologues and that no $^{87}RbF^+$ is transmitted to interfere with $^{87}SrF^+$. The first assumption is based on the fact that most of isotope fractionation in ICPMS occurs in the plasma due to a change in the gas regime from a thermalized state to laminar flow,[48] thus well before the analyte, here Sr, enters the CRC. The second assumption is at the core of the CRC technology, and we will see that it holds for SF_6, which allows Sr^+, but not Rb^+, to be converted into a F-based compound. Sample normalized $^{87}SrF/^{86}SrF$ ratios were then corrected from temporal instrumental drift using sample-standard bracketing to obtain corrected (s,c) $^{87}SrF/^{86}SrF$ ratios following the equation,

$$\left(\frac{^{87}SrF}{^{86}SrF}\right)_{s,c} = \left(\frac{^{87}SrF}{^{86}SrF}\right)_{s,n} \times \frac{\left(\frac{^{87}SrF}{^{86}SrF}\right)_{r,t}}{\frac{1}{2}\left(\frac{^{87}SrF}{^{86}SrF}\right)_{r-1,n} + \frac{1}{2}\left(\frac{^{87}SrF}{^{86}SrF}\right)_{r+1,n}} \quad (3)$$

where $(^{87}SrF/^{86}SrF)_{r,t}$ refers to the true ratio of the reference standard solution SRM-987 (National Institute of Standards and Technology, Gaithersburg, MD) and $(^{87}SrF/^{86}SrF)_{r,n}$ to the normalized value of the reference standard solution SRM-987.

For the Neoma without the CRC, the Neptune, and the Nu Plasma instruments, it is necessary to correct $^{87}Sr^+$ from the $^{87}Rb^+$ isobaric interference using the equation,

$$^{87}Sr_m = {}^{87}Sr_m - {}^{85}Rb_m \times \left(\frac{^{87}Rb}{^{85}Rb}\right)_t \times \left(\frac{M^{87}Rb}{M^{85}Rb}\right)^{\beta_{Sr}} \quad (4)$$

where $M^{87,85}Rb$ correspond to the atomic masses of the corresponding isotopes and $(^{87}Rb/^{85}Rb)_t$ the natural abundance of the $^{87}Rb/^{85}Rb$ ratio (0.3856). Normalized $^{87}Sr/^{86}Sr$ ratios were corrected from temporal instrumental drift using the sample-standard bracketing method adapted from eqn (3). Sample and standard solutions were diluted to reach 200 ppb. All statistical analyses were performed using R software.[49]

3 Results and discussion

3.1 MS/MS prefiltering performances

3.1.1 The double-Wien filter. The axial mass (m_0) was set at half the mass dispersion between ^{84}Sr and ^{88}SrF, *i.e.*, at 96 amu, and the adjustable slit was open at 50 or 70% (Table 2). Using the SCP33MS solution allows monitoring the effects of the double-Wien filter on the overall transmission, which is outlined in Fig. 1 as a blue envelope of the bandpass window. As already reported,[9] increasing the B value steepens the low mass edge of the bandpass window and augments the intensity of the central masses, probably thanks to the removal of Ar^+ ions that produce significant defocusing (Fig. 1A–C). At $B = 10\%$ (Fig. 1A), U is still partially and Pb fully transmitted, while masses at ~50 amu are already efficiently deflected. At $B = 30\%$ (Fig. 1B), a bandpass window from 70 to 142 amu is selected, which narrows from 80 to 124 amu at $B = 50\%$ (Fig. 1C). At both Bremen and Lyon, the best configuration was found to be a combination of a magnetic field B value at 50%, an electrostatic field E value at ~300 V, and a slit aperture S value ranging from 50% to 70% (Table 2), similar to those used for ^{87}Rb–^{87}Sr analyses.[39]

3.1.2 The collision/reaction cell. Isotope measurements by multi-collection imply that a range of masses, here from 80 to

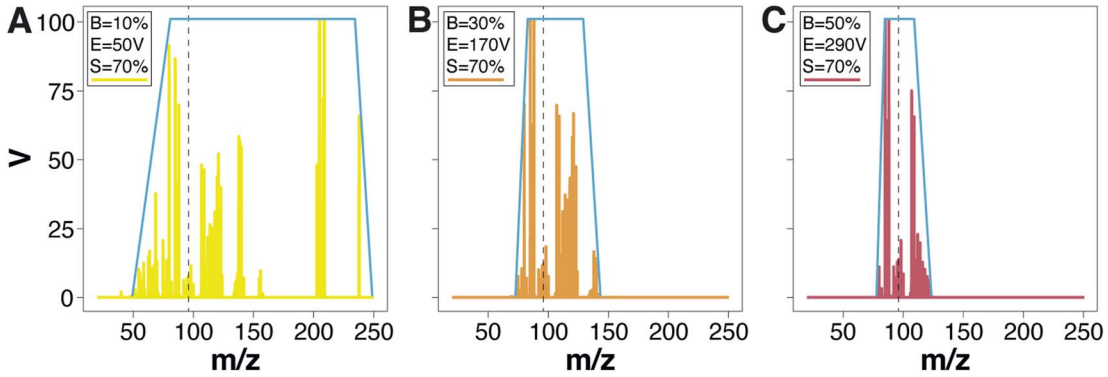

Fig. 1 Overall signal intensities for a mass scan with $m_0 = 98$ from 20 to 250 m/z for various values of magnetic field (B, %) values of the double-Wien filter. Increasing the magnetic field necessitates increasing the electrostatic field (E, V) to keep the E/B ratio constant. The adjustable slit aperture (S) is maintained at 70% open. (A) $B = 10\%$, $E = 50$ V. (B) $B = 30\%$, $E = 170$ V. (C) $B = 50\%$, $E = 290$ V. For each configuration, the envelope of the selected bandpass window is shown in blue. The bandpass window centers relative to m_0, and its sides steepen when increasing the B value. Amplifier of the axial collector was set at 10^{11} Ω.

124 amu (at $B = 50\%$), enter the CRC simultaneously. This greatly differs from tandem MS/MS with triple-quadrupole technology, which selects and transmits, or not, ions at one amu mass resolution. This is why it is important to upstream prefilter the ion beam thanks to the double-Wien filter to reduce potential spectral and matrix interferences and permit much better resolution and control of subsequent effects in the CRC. In multi-collection, it is thus possible to monitor the residual intensities of ions that have not reacted in the CRC, as well as those of ions that have reacted and the interfering species that have been potentially created. Of note, the commercial Neoma at Lyon has a full mass dispersion of 22%, allowing the measurements of Sr isotope compositions from 85 to 107 amu in static mode (Table 3), whereas the precommercial Neoma at Bremen needs the peak jumping mode to proceed with those isotopic measurements[39] (Table 3).

We tested SF_6 and N_2O as reaction gases and monitored the intensity of Sr isotopes in the SRM-987 solution at 200 ppb to deduce the transmission rate (as the intensities ratio of the Sr isotopes without gas over that of the residual Sr isotopes with a given gas) and the conversion rate (for a given gas, as the intensities ratio of the reacted Sr isotopes over that of the residual Sr isotopes, config. §1, Table 3). The results are shown in Fig. 2 as mass scans from 82.5 to 108.5 amu for a configuration with no gas (Fig. 2A), SF_6 at 0.12 ml min^{-1} (Fig. 2B), and N_2O at 0.11 ml min^{-1} (Fig. 2C). The scans are configurated to include 10 000 measurements so that each peak exhibits a distinct plateau and interferences can easily be detected. The introduction of SF_6 decreases the transmission by half (56.2%, 55.5%, and 54.3% for ^{86}Sr, ^{87}Sr, and ^{88}Sr, respectively, residual ^{84}Sr being undetectable) and allows the conversion of more than 95% of Sr into SrF (95.3%, 95.4%, and 95.6% for ^{86}Sr, ^{87}Sr, and ^{88}Sr, respectively). In addition to the formation of sulfur tetrafluoride at 108 amu, the introduction of SF_6 generates an isobaric interference of $^{32}S^{19}F_3{}^{16}O^+$ on the high-mass shoulder of ^{88}SrF at 107 amu (Fig. 3A), which tends to shrink over time but remains significant (Fig. S1A†). The measurement of the ^{88}SrF interference-free intensity can however be performed at the middle of the plateau towards the low-mass shoulder (Fig. S1B†). Repeated measurements of the $^{87}SrF/^{86}SrF$ ratio in the SRM-987 solution yields a value of 0.71023 ± 0.00005 (±2SD, $n = 15$) similar to that measured by thermal ionization mass spectrometry (TIMS, 0.71025 ± 0.00002 (±2SD, $n = 25$ (ref. 50)). The introduction of N_2O alters only slightly the transmission (93.1%, 94.5%, 93.5%, and 89.5% for ^{84}Sr, ^{86}Sr, ^{87}Sr, and ^{88}Sr, respectively) and allows the conversion of more than 85% of Sr into SrO^+ (83.3%, 80.1%, 86.9%, and 89.9% for ^{84}Sr, ^{86}Sr, ^{87}Sr, and ^{88}Sr, respectively). The introduction of N_2O in the CRC therefore leads to an expected better transmission rate than SF_6 (ref. 38) and a reasonable conversion rate, but is associated with the formation of N-based interfering species (Fig. 2C). The presence of a peak of a tenth of mV at 101 amu reveals the formation of $^{87}Sr^{14}N^+$, implying that $^{84}Sr^{16}O^+$ at 100 amu is interfered with $^{86}Sr^{14}N^+$ and that $^{86}Sr^{16}O^+$ at 102 amu is interfered with $^{88}Sr^{14}N^+$ (Fig. 2C). In addition, N_2O produces peaks at 105, 106 and 107 amu (Fig. 2C). The peak at 106 amu most probably corresponds to $^{88}Sr^{18}O^+$ because its average intensity (0.021 V) is 0.26 times that of $^{88}Sr^{16}O^+$ at 104 amu (12.4 V), close to the $^{18}O/^{16}O$ natural abundance of 0.2. We actually have no firm explanation regarding the peaks at 105 amu (0.265 V) and 107 amu (0.0057 V), but a reasonable hypothesis is that they correspond to $^{88}Sr^{16}O^+$ and $^{88}Sr^{18}O^+$ H-based compounds. Indeed, the 104/105 and 106/107 intensity ratios are 46.8 and 46.5, respectively, suggesting that a common mechanism is at work to create the signals measured at 105 and 107 amu. If true, this suggests that the H-based interference also exists at 103 amu on $^{87}Sr^{16}O^+$ ($^{86}Sr^{16}OH^+$) and at 104 amu on $^{88}Sr^{16}O^+$ ($^{87}Sr^{16}OH^+$). We also found that residual $^{88}Sr^+$ is interfered on the high-mass shoulder by $^{40}ArO_3{}^+$ (Fig. 3B), which is surprising because Ar^+ should not be transmitted at all by the double-Wien filter given that m_0 is set at 96 amu, *i.e.*, 46 amu away from Ar. Scrutinizing the $^{88}SrO^+$ peak at 104 amu using the extra-high resolution mode (XHR, mass resolving power ~17 000) reveals that this interference is no longer detected

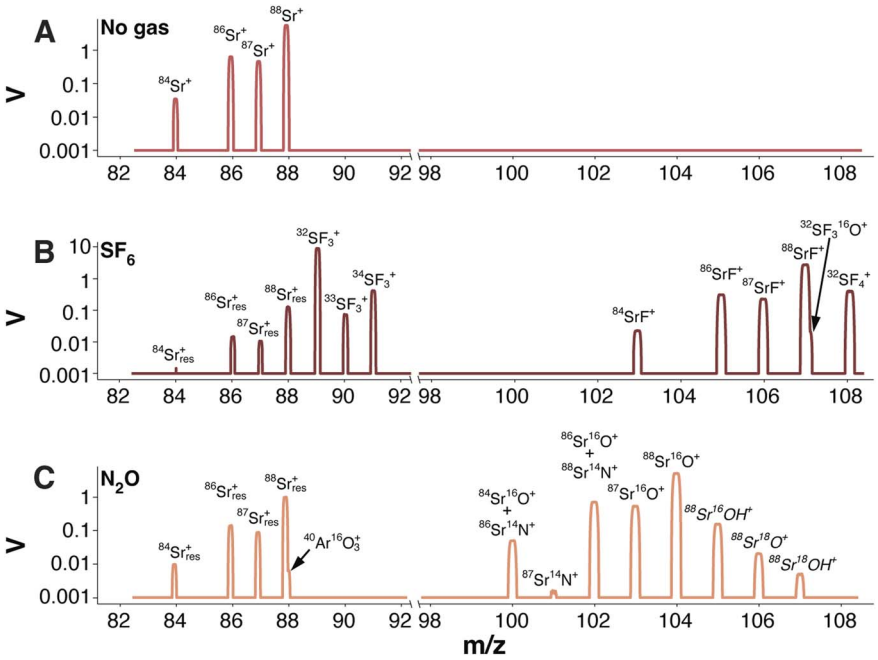

Fig. 2 Overall signal intensities for a mass scan with $m_0 = 98$ from 82.5 to 108.5 m/z for various CRC configurations with $B = 50\%$, $E = 290$ V, and $S = 70\%$. (A) No gas in the CRC. (B) SF_6 at 0.12 ml min^{-1}. (C) N_2O at 0.11 ml min^{-1}. Ions are indicated and are in italic when the identification is uncertain. Amplifier of the axial collector was set at 10^{11} Ω.

when Sr has reacted with N_2O in the CRC (Fig. 3B). Finally, measurement of the $^{87}SrO/^{86}SrO$ ratio in the SRM-987 solution gives too high values (~0.725), whatever the CRC bias value. Given all the detected interferences on Sr isotopes produced by the introduction of N_2O and the systematic failure to measure an accurate $^{87}SrO/^{86}SrO$ ratio in the SRM-987 solution using the expected normal mass bias correction prompt us to use SF_6 as the reaction gas in the course of the present work.

3.2 Measurements of $^{87}SrF/^{86}SrF$ in solution

We first challenged the capability of the Neoma MS/MS to separate online Sr from Rb by measuring the $^{87}SrF/^{86}SrF$ ratio (config. §2a, Table 3) in raw solutions in a suite of geological reference materials without prior Sr extraction (exp #1, Table 1). All the results are given in Table S1.† The sensitivity is ~50 V ppm^{-1} for ^{88}SrF with a blank level in 2% HNO_3 of 6 mV (Table 2). The SRM-987 yields an average $^{87}SrF/^{86}SrF$ ratio of 0.71025 ± 0.00005 (±2SD, n = 19), matching that generally expected.[50] No RbF^+ is detectable, but it is noteworthy that the Rb/Sr ratio is generally low (<0.1) in this suite of magmatic or intrusive rock CRMs.[41] The measurements of the $^{87}SrF/^{86}SrF$ ratio in raw solutions yield values that perfectly match recommended ratios (Fig. 4). The precision of the measurements ranges from 2×10^{-5} to 10^{-4} with an average value of 7×10^{-5} (±2SD). These results are similar, at the lowest level, to those obtained by MC-ICPMS with prior Sr extraction (Table S1†). We found no association between the value of the measured

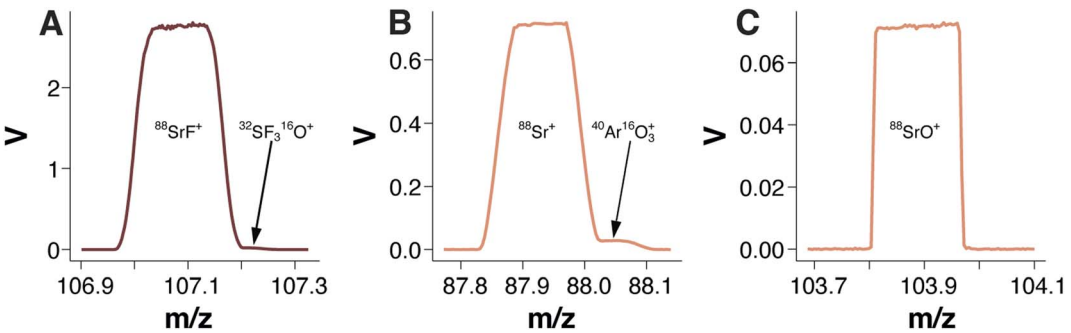

Fig. 3 Peak scans using the low ($\Delta M/M$ ~3000) resolution slit for selected peaks in the SRM-987 solution at 200 ppb. (A) Isobaric $^{32}S^{19}F_3{}^{16}O^+$ interference on the high-mass shoulder of $^{88}Sr^{19}F^+$ with SF_6 at 0.12 ml min^{-1}. Further peak scans are shown in Fig. S1.† (B) Isobaric $^{40}Ar^{16}O_3{}^+$ interference on the high-mass shoulder of residual $^{88}Sr^+$ with N_2O at 0.11 ml min^{-1}. (C) This interference is no longer present at 107 amu as shown by the use of the XHR ($\Delta M/M$ ~17 000) resolution slit.

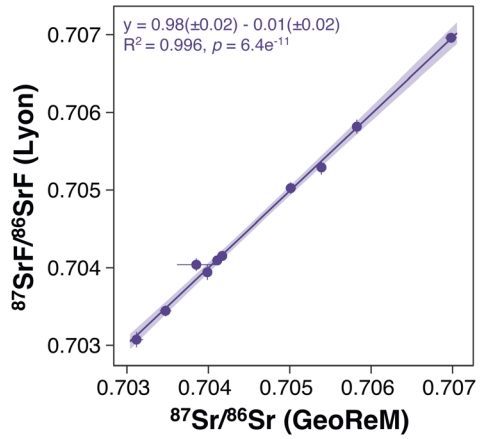

Fig. 4 Correlation between the measured $^{87}SrF/^{86}SrF$ ratio of CRMs (exp. #1, Table 1) raw solutions of and their certified $^{87}Sr/^{86}Sr$ value as provided in the GeoReM database[41] and given in Table S1.†

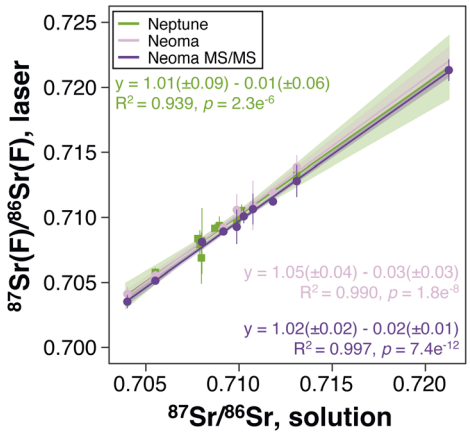

Fig. 5 Correlation between the $^{87}SrF/^{86}SrF$ ratio (using the Neoma MS/MS) and the $^{87}Sr/^{86}Sr$ ratio (using the Neoma or the Neptune) of sintered powder samples and monocrystalline FAP (exp. #2, Table 1) measured by laser ablation and the $^{87}Sr/^{86}Sr$ ratio measured in solution after Sr purification. All values are given in Table S1.†

standard error and the Rb and/or Sr content (Table S1†). The slope of 0.98 ± 0.02 and the offset at origin of −0.01 ± 0.02 of the linear regression indicate that the $^{87}SrF/^{86}SrF$ ratios have been measured without any matrix effects. Only one sample, BE-N (Table 1), is slightly offset, but this CRM has the greatest uncertainty (±0.0024, 2SD, $n = 5$) on the GeoReM database due to the presence of an outlier $^{87}Sr/^{86}Sr$ value measured on leached sample.[41]

3.3 Measurements of $^{87}SrF/^{86}SrF$ with laser ablation

3.3.1 Accuracy of the $^{87}Sr/^{86}Sr$ *vs.* $^{87}SrF/^{86}SrF$ ratios. We second challenged the capability of the Neoma MS/MS to separate online Sr from Rb by measuring the $^{87}Sr/^{86}Sr$ (config. §3a, Table 3) and the $^{87}SrF/^{86}SrF$ ratios (config. §2b, Table 3) in a suite of sintered powder samples using LA (exp #2, Table 1). For comparison, we also include $^{87}Sr/^{86}Sr$ values that were measured on a Neptune coupled to the LA system (config. §3b, Table 3). As reference values, the $^{87}Sr/^{86}Sr$ ratios were measured according to the published method after Sr chromatographic purification in solution mode. Here, the values of SRM-987 were measured at 0.71027 ± 0.00005 (±2 SD, $n = 97$) on the Nu plasma config. §4, Table 3). The All the results are given in Table S1.† For similar LA settings (Table 2), the transmission of ^{88}Sr is ~8 mV ppm^{-1} with SF_6, while it is about twice that without, whether for the Neoma or the Neptune (Table 2). The results are shown in Fig. 5 and indicate that the $^{87}Sr/^{86}Sr$ ratio of the samples is generally measured accurately in the LA mode in the present study, whatever the instrument or the configuration. This is probably due to the good sensitivity of the overall setups, which yield ^{88}Sr signals ranging from 1.2 V to 44.2 V with the Neptune and the Neoma without SF_6, and from 0.4 V to 53.3 V with the Neoma with SF_6. However, the uncertainties associated with the best fit correlation between the $^{87}Sr/^{86}Sr$ or $^{87}SrF/^{86}SrF$ ratios measured with LA *vs.* the $^{87}Sr/^{86}Sr$ ratio measured in solution, are greater with the Neptune compared to the Neoma without SF_6, which in turn are greater compared to the Neoma with SF_6. This is illustrated by the resulting *p*-value associated with the Pearson correlation coefficient, which decreases from 2.3 × 10^{-6} for the Neptune to 1.8 × 10^{-8} for the Neoma without SF_6 and 7.4 × 10^{-12} for the Neoma with SF_6 (Fig. 5). Overall, these results demonstrate that there is a slight but added value to measuring the $^{87}SrF/^{86}SrF$ ratio instead of the $^{87}Sr/^{86}Sr$ ratio, despite a loss of transmission by a factor 2.

3.3.2 Variation of the $^{87}Sr/^{86}Sr$ *vs.* $^{87}SrF/^{86}SrF$ ratios. To get insight into the influence of the CRC on the analysis of the Sr radiogenic isotope ratio, we performed two adjacent rasters in a fossil tooth (exp. #3, Table 1), a first without SF_6 (config. §3a, Table 2) and a second with SF_6 (config. §2b, Table 2). The results show that Rb, which is present as several mV of ^{85}Rb, for example, in the first millimeter of the profile (Fig. 6A), is no longer transmitted when SF_6 is added (Fig. 6B). Expectedly, the ^{88}Sr and the ^{88}SrF signals show similar variations along both profiles (Fig. 6C and D). A comparison of the intensities along the profiles yields a factor of 0.56 between the ^{88}Sr and the ^{88}SrF signals (Fig. S2†). Factors of 0.60 and 0.62 are calculated between the ^{87}Sr and the ^{87}SrF signals and between the ^{86}Sr and the ^{86}SrF signals, respectively, consistent with that between the ^{88}Sr and the ^{88}SrF signals. The $^{87}Sr/^{86}Sr$ and $^{87}SrF/^{86}SrF$ ratios have similar values but also display comparable variations (Fig. 6E and F). However, a close inspection of the results reveals that the variability of the measurements is slightly higher with SF_6 (Fig. 6A) than without SF_6 (Fig. 6B). Indeed, the standard deviation associated with the calculation of the moving average is ±0.0003 (±1 SD) and ±0.0004 (±1 SD) for the $^{87}Sr/^{86}Sr$ and $^{87}SrF/^{86}SrF$ ratios, respectively. Despite the slightly higher scattering of the measurements with SF_6, the variations of Sr isotopes are more resolved than without SF_6. Fig. S3† shows that departures from the identity line are more frequent, notably between ~3.5 mm and ~5.5 mm. More work on studying the systematics of variations of the $^{87}Sr/^{86}Sr$ and the $^{87}SrF/^{86}SrF$ ratios will be of interest for best constraining reconstructions of human and animal past mobility.

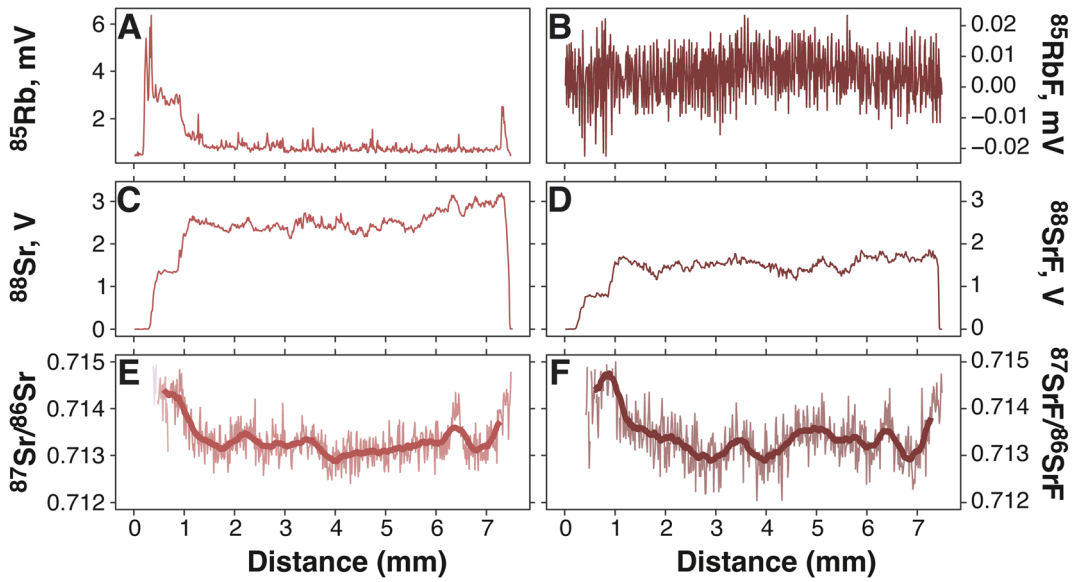

Fig. 6 Laser ablation profiles in a fossil tooth (exp. #3, Table 1), (A) ^{85}Rb intensity without SF_6, (B) $^{85}Rb{\cdot}F$ intensity with SF_6, (C) ^{88}Sr intensity without SF_6, (D) ^{88}Sr intensity with SF_6, (E) $^{87}Sr/^{86}Sr$ ratio without SF_6, (F) $^{87}SrF/^{86}SrF$ ratio with SF_6. Reaction gas SF_6 is set at 0.12 L min^{-1}.

4 Conclusions

For high-precision isotope measurements by multi-collection, ions with different masses must enter a CRC simultaneously, potentially creating many interfering products with the present gas. This can be partially overcome by prefiltering the ion beam, which is achieved in the Neoma MS/MS with a double-Wien filter. However, even with optimized settings of the double-Wien filter, a bandpass window of about 40 mass units will ever enter the CRC. This can represent a serious limitation for CRC-MC-ICPMS to measure high-precision isotope compositions if the analyte is not priorly purified by ion-exchange chromatography, such as when using laser ablation. Here, we aimed at measuring the Sr radiogenic isotope compositions in solution without prior Sr purification and with laser ablation with the Neoma MS/MS. We showed that introducing N_2O creates ^{14}N- and ^{18}O-based isobaric interferences on $Sr^{16}O$ products. In contrast, reaction with F, introduced as SF_6, produces a neater spectrum of ^{19}F-based Sr isotope products. Thus, using SF_6, we show that mass fractionation follows the expected exponential law, allowing to measure accurate $^{87}SrF/^{86}SrF$ ratios in raw solutions of geological CRM with a precision equivalent to that obtained by MC-ICPMS with prio Sr extraction. Using laser ablation with SF_6 slightly improves the performance of the analyses compared to without, despite a decrease of about half of the transmission.

Conflicts of interest

There are no conflicts to declare.

Acknowledgements

The authors are grateful to O. Boeuf, C. Kassegne and J. E. M. Martin for providing fossil samples, E. Albalat and D. Guiserix for helping in the isotopic measurements, the staff at Elemental Scientific Lasers for providing a laser and technical support as part of the formal collaboration with ENS-Lyon, and the Institut National des Sciences de l'Univers (INSU) of the CNRS, the LABEX Lyon Institute of Origins (ANR-10-LABX-0066) of the Université de Lyon, the Fonds Recherche of the Ecole Normale Supérieure de Lyon, and the Laboratoire de Géologie de Lyon: Terre, Planètes, Environments, for their financial support.

References

1 S. D. Tanner, V. I. Baranov and D. R. Bandura, *Spectrochim. Acta, Part B*, 2002, **57**, 1361–1452.
2 G. C. Eiden, C. J. Barinaga and D. W. Koppenaal, *J. Anal. At. Spectrom.*, 1996, **11**, 317–322.
3 M. Rehkämper and K. Mezger, *J. Anal. At. Spectrom.*, 2000, **15**, 1451–1460.
4 Y. Ku and S. B. Jacobsen, *Sci. Adv.*, 2020, **6**, eabd0511.
5 H. Chen, N. J. Saunders, M. Jerram and A. N. Halliday, *Chem. Geol.*, 2021, **578**, 120281.
6 F. Moynier, Y. Hu, K. Wang, Y. Zhao, Y. Gérard, Z. Deng, J. Moureau, W. Li, J. I. Simon and F.-Z. Teng, *Chem. Geol.*, 2021, **571**, 120144.
7 G. Craig, H. Wehrs, D. G. Bevan, M. Pfeifer, J. Lewis, C. D. Coath, T. Elliott, C. Huang, N. S. Lloyd and J. B. Schwieters, *Anal. Chem.*, 2021, **93**, 10519–10527.
8 D. Bevan, C. D. Coath, J. Lewis, J. Schwieters, N. Lloyd, G. Craig, H. Wehrs and T. Elliott, *J. Anal. At. Spectrom.*, 2021, **36**, 917–931.
9 P. Télouk, E. Albalat, B. Bourdon, F. Albarède and V. Balter, *J. Anal. At. Spectrom.*, 2023, **38**, 1973–1983.
10 W. Dai, F. Moynier, M. Paquet, J. Moureau, B. Debret, J. Siebert, Y. Gerard and Y. Zhao, *Chem. Geol.*, 2022, **590**, 120688.

11 B.-Y. Gao, B.-X. Su, W.-J. Li, M. Yuan, J. Sun, Y. Zhao and X. Liu, *J. Anal. At. Spectrom.*, 2022, **37**, 2111–2121.
12 Z. T. Eriksen and S. B. Jacobsen, *Earth Planet. Sci. Lett.*, 2022, **593**, 117665.
13 S. An, J. Chen, S. Boschi and W. Li, *Anal. Chem.*, 2023, **95**, 2140–2145.
14 M.-M. Cui, F. Moynier, B.-X. Su, W. Dai, Y. Hu, D. Rigoussen, B. Mahan and M. Le Borgne, *Metallomics*, 2023, **15**, mfad033.
15 C. A. Parendo, S. B. Jacobsen and T. Plank, *Geochim. Cosmochim. Acta*, 2022, **337**, 166–181.
16 J. Wang, D.-M. Tang, B.-X. Su, Q.-H. Yuan, W.-J. Li, B.-Y. Gao, K.-Y. Chen, Z.-A. Bao and Y. Zhao, *J. Anal. At. Spectrom.*, 2022, **37**, 1869–1875.
17 G. J. Wasserburg, D. A. Papanastassiou and H. G. Sanz, *Earth Planet. Sci. Lett.*, 1969, **7**, 33–43.
18 F. A. Podosek, C. A. Prombo, S. Amari and R. S. Lewis, *ApJ*, 2004, **605**, 960.
19 W. M. White, J.-G. Schilling and S. R. Hart, *Nature*, 1976, **263**, 659–663.
20 S. M. McLennan, S. R. Taylor, M. T. McCulloch and J. B. Maynard, *Geochim. Cosmochim. Acta*, 1990, **54**, 2015–2050.
21 J. Veizer, D. Buhl, A. Diener, S. Ebneth, O. G. Podlaha, P. Bruckschen, T. Jasper, C. Korte, M. Schaaf, D. Ala and K. Azmy, *Palaeogeogr., Palaeoclimatol., Palaeoecol.*, 1997, **132**, 65–77.
22 S. El Meknassi, G. Dera, T. Cardone, M. De Rafélis, C. Brahmi and V. Chavagnac, *Geology*, 2018, **46**, 1003–1006.
23 J. E. Martin, U. Deesri, R. Liard, A. Wattanapituksakul, S. Suteethorn, K. Lauprasert, H. Tong, E. Buffetaut, V. Suteethorn, G. Suan, P. Telouk and V. Balter, *Paleobiology*, 2015, **42**, 143–156.
24 A. Sillen and V. Balter, *J. Hum. Evol.*, 2018, **114**, 118–130.
25 A. Hermann, P. Gutiérrez, C. Chauvel, R. Maury, C. Liorzou, E. Willie, I. Phillip, R. Forkel, C. Rzymski and S. Bedford, *Sci. Adv.*, 2023, **9**, eadf4487.
26 B. A. Stewart, Y. Zhao, P. J. Mitchell, G. Dewar, J. D. Gleason and J. D. Blum, *Proc. Natl. Acad. Sci. U. S. A.*, 2020, **117**, 6453–6462.
27 E. Balboni, N. Jones, T. Spano, A. Simonetti and P. C. Burns, *Appl. Geochem.*, 2016, **74**, 24–32.
28 E. J. Bartelink, A. T. Mackinnon, J. R. Prince-Buitenhuys, B. J. Tipple and L. A. Chesson, in *Handbook of Missing Persons*, ed. S. J. Morewitz and C. Sturdy Colls, Springer International Publishing, Cham, 2016, pp. 443–462.
29 J. Sun, R. Yu, Y. Yan, G. Hu, Q. Qiu, S. Jiang, J. Cui, X. Wang and C. Ma, *Chemosphere*, 2020, **246**, 125638.
30 B. Saar de Almeida, L. Fedele, M. D'Antonio, V. Morra, M. Mercurio, R. Stevenson and D. Widory, *Isot. Environ. Health Stud.*, 2023, 1–22.
31 L. J. Moens, F. F. Vanhaecke, D. R. Bandura, V. I. Baranov and S. D. Tanner, *J. Anal. At. Spectrom.*, 2001, **16**, 991–994.
32 P. Cheng, G. K. Koyanagi and D. K. Bohme, *Anal. Chim. Acta*, 2008, **627**, 148–153.
33 T. Zack and K. J. Hogmalm, *Chem. Geol.*, 2016, **437**, 120–133.
34 E. Bolea-Fernandez, S. J. M. V. Malderen, L. Balcaen, M. Resano and F. Vanhaecke, *J. Anal. At. Spectrom.*, 2016, **31**, 464–472.
35 A. Redaa, J. Farkaš, S. Gilbert, A. S. Collins, B. Wade, S. Löhr, T. Zack and D. Garbe-Schönberg, *J. Anal. At. Spectrom.*, 2021, **36**, 322–344.
36 D. Rösel and T. Zack, *Geostand. Geoanal. Res.*, 2022, **46**, 143–168.
37 L. Gorojovsky and O. Alard, *J. Anal. At. Spectrom.*, 2020, **35**, 2322–2336.
38 K. J. Hogmalm, T. Zack, A. K.-O. Karlsson, A. S. L. Sjöqvist and D. Garbe-Schönberg, *J. Anal. At. Spectrom.*, 2017, **32**, 305–313.
39 N. Dauphas, T. Hopp, G. Craig, Z. J. Zhang, M. C. Valdes, P. R. Heck, B. L. A. Charlier, E. A. Bell, T. M. Harrison, A. M. Davis, L. Dussubieux, P. R. Williams, M. J. Krawczynski, C. Bouman, N. S. Lloyd, D. Tollstrup and J. B. Schwieters, *J. Anal. At. Spectrom.*, 2022, **37**, 2420–2441.
40 T. Tacail, P. Télouk and V. Balter, *J. Anal. At. Spectrom.*, 2015, **31**, 152–162.
41 K. P. Jochum, U. Nohl, K. Herwig, E. Lammel, B. Stoll and A. W. Hofmann, *Geostand. Geoanal. Res.*, 2005, **29**, 333–338.
42 L. Rey, T. Tacail, F. Santos, S. Rottier, G. Goude and V. Balter, *Chem. Geol.*, 2022, **587**, 120608.
43 M. Weber, F. Lugli, K. P. Jochum, A. Cipriani and D. Scholz, *Geostand. Geoanal. Res.*, 2018, **42**, 77–89.
44 V. Balter, J. –F. Saliège, H. Bocherens and A. Person, *Archaeometry*, 2002, **44**, 329–336.
45 V. Balter, A. Person, N. Labourdette, D. Drucker, M. Renard and B. Vandermeersch, *C. R. Acad. Sci. Ser. II*, 2001, **332**, 59–65.
46 D. Guiserix, E. Albalat, H. Ueckermann, P. Davechand, L. M. Iaccheri, G. Bybee, S. Badenhorst and V. Balter, *Chem. Geol.*, 2022, **606**, 121000.
47 M. Rivollat, A. B. Rohrlach, H. Ringbauer, A. Childebayeva, F. Mendisco, R. Barquera, A. Szolek, M. Le Roy, H. Colleran, J. Tuke, F. Aron, M.-H. Pemonge, E. Späth, P. Télouk, L. Rey, G. Goude, V. Balter, J. Krause, S. Rottier, M.-F. Deguilloux and W. Haak, *Nature*, 2023, **620**, 600–606.
48 F. Albarède, E. Albalat and P. Télouk, *J. Anal. At. Spectrom.*, 2015, **30**, 1736–1742.
49 *R.: The R Project for Statistical Computing*, **https://www.r-project.org/**, (accessed April 14, 2023).
50 J.-M. Brazier, A.-D. Schmitt, E. Pelt, D. Lemarchand, S. Gangloff, T. Tacail and V. Balter, *Geostand. Geoanal. Res.*, 2020, **44**, 331–348.